The influence of aluminium on the overall properties of SnO$_2$-based varistors

Rodrigo Parra · Yves Maniette · José A. Varela · Miriam S. Castro

Abstract The influence of aluminium on the development of the microstructure and on the electrical behaviour of the SnO$_2$ · Co$_3$O$_4$ · Nb$_2$O$_5$ typical varistor system was studied. Two sources of Al were used, alumina (Al$_2$O$_3$) and boehmite (AlO(OH)). The microstructural features were characterised with scanning (SEM) and transmission (TEM) electron microscopies. The different phases present in the studied samples were also studied with XRD, EDS and electron diffraction patterns of selected areas (SAED). Particles containing Sn, Co, Al, and O were unveiled with TEM. Impedance spectroscopy measurements and current density versus electric field characteristics revealed superior electrical properties for samples with AlO(OH). The higher non-linearity ($\alpha = 19$) was achieved with the addition of 0.1% mol of boehmite. The influence of the secondary phases on the electrical properties is also addressed in this work.

Introduction

Metal oxide varistors are electroceramic devices commonly used as surge arrestors in electronic circuits and power systems. They can be used over wide ranges of voltages and currents according to their specific properties. The most widely studied class of varistor is manufactured by sintering ZnO with small additions of metal oxides such as CoO, Bi$_2$O$_3$, Sb$_2$O$_3$ and MnO [1–3]. The resultant product is a polycrystalline ceramic in which spinel and pyrochlore phases may be present [4, 5]. These devices exhibit highly non-linear voltage–current characteristics by virtue of which they act as insulators or conductors depending on the applied voltage.

A new varistor system based on SnO$_2$ has been introduced by Pianaro et al. in 1995 [6]. The effects on the global properties of SnO$_2$ varistors of Co$_3$O$_4$, CoO, ZnO, Sb$_2$O$_3$, Nb$_2$O$_5$, Fe$_2$O$_3$ and La$_2$O$_3$, among other metal oxides, have been systematically studied. It has been determined that Co, Mn and Zn oxides create charged oxygen vacancies at sintering temperatures that enhance diffusion and mass transport mechanisms leading to densification and grain growth [7, 8]. Conversely, Sb$_2$O$_3$ and Nb$_2$O$_5$ decrease the sintering rate of SnO$_2$ when forming solid solution and increase the electrical conductivity [9–10]. Moreover, trivalent metal oxides (Fe$_2$O$_3$, La$_2$O$_3$, Al$_2$O$_3$ and Pr$_2$O$_3$) have been found to improve the non-linear properties of SnO$_2$-based varistors [8, 11–15]. The simple microstructure, consisting generally in one phase under X-ray resolution, is the key characteristic of these electroceramics. However, the presence of secondary phases in the microstructure of SnO$_2$-based varistors has been recently reported [14, 16].

The purpose of the present work is to determine the effects of the addition of aluminium on the microstructure and on the electrical properties of the SnO$_2$ · Co$_3$O$_4$ · Nb$_2$O$_5$ varistor system. In order to gain advantage of the proposed study, two different sources of aluminium—Al$_2$O$_3$ and AlO(OH)—were tested.

R. Parra (✉) · M. S. Castro
Instituto de Investigaciones en Ciencia y Tecnología de Materiales, (INTEMA, CONICET-UNMdP), J.B. Justo 4302, B7608FDQ Mar del Plata, Argentina
e-mail: rparra@fi.mdp.edu.ar

Y. Maniette · J. A. Varela
Instituto de Química, UNESP, PO Box 355, 14801-970 Araraquara, Brazil

Experimental procedure

Analytical grades of SnO_2, Co_3O_4, Nb_2O_5, Al_2O_3 and AlO(OH) were used as precursors for SnO_2-based varistors. Selected compositions are listed in Table 1. Oxides were mixed in 2-propanol stirring in a high-speed turbine at 6,000 rpm for 5 min. The boehmite was attacked with an acetic acid solution in order to obtain a gel that was finally mixed with the SnO_2 along with the other additives. After drying the suspensions at 65 °C during 48 h, the powders were sieved through a 43 μm mesh screen to disintegrate the possible agglomerates of particles. Powders were uniaxially pressed (150 kg·cm^{-2}) into discs of a thickness around 1 mm and 12 mm in diameter. The obtained discs were sintered in a stationary air atmosphere at 1300 °C for 2 h with heating and cooling rates of 3 °C/min in a Carbolite RHF17/6S furnace.

The apparent density of sintered samples was determined through the Archimedes method. X-ray diffraction analysis (XRD) was carried out by means of a Philips 1830/00 diffractometer running with CoK_{α} radiation at 40 kV and 30 mA in order to establish the unit cell volume and the phases present in the final microstructures. The unit cell parameters a and c of the tetragonal lattice of SnO_2 were calculated from the following expressions:

$$\frac{1}{d^2} = \frac{(h^2 + k^2)}{a^2} + \frac{l^2}{c^2}, \tag{1}$$

where d is the interplanar spacing and h, k and l are the associate Miller indexes. Considering the peaks (110) and (101) in the diffraction pattern, those of major intensity, it turns out that

$$a = \sqrt{2}d_{(110)} \tag{2}$$

and

$$c = \left(\frac{1}{d_{(101)}^2} - \frac{1}{2d_{(110)}^2}\right)^{-1/2}. \tag{3}$$

Finally, the volume of the unit cell V is equal to a^2c. For each set of compositions, measurements on three different samples were carried out.

The microstructures were characterised by scanning electron microscopy (SEM) in a Jeol JSM-6460LV microscope under the secondary electrons mode (SE), and by transmission electron microscopy (TEM) in a Philips CM200 instrument operating at 200 kV. Both SEM and TEM instruments were equipped with EDS systems for energy dispersive X-ray analysis. Samples for SEM were polished with SiC paper and diamond pastes and thermally etched 50 °C below the sintering temperature. Average grain sizes were determined through the method of the intercepts [17]. Samples for TEM were prepared by cutting discs of plane and parallel faces of 3 mm in diameter using an ultrasonic cutter. The discs were ground down to a thickness of 100 μm and then dimpled by means of an SBT Dimple Grinder Model 515 to get a 30-μm thickness at the centre of the specimens. Finally, large electron transparent regions were achieved by ion milling performed in a Bal-Tec RES010 ion mill operating at 4 kV and 1.5 mA on each gun. Electron diffraction patterns were obtained from selected areas.

Silver electrodes were painted on the plane surfaces of the sintered samples for electrical characterisation. A Keithley 237 high voltage source-measure unit was used to obtain the current density (J) versus electric field (E) characteristics at room temperature. Assuming the grain boundary breakdown value to be compatible with the SnO_2 band gap of 3.5 V, the percentage of electrically active barriers (EAB) in each sample can be determined as

$$\%EAB = \frac{V_b}{3.5} 100, \tag{4}$$

with

$$V_b = V_r \frac{d}{e}, \tag{5}$$

where V_b is the breakdown voltage per barrier, V_r is the breakdown voltage of the device measured at 1 mA cm^{-2}, e is the sample thickness and d the average grain size [18]. Impedance spectroscopy (IS) measurements were carried out by means of an HP4284A LRC meter with an amplitude voltage of 0.5 V in the frequency range of 20 Hz–1 MHz. Curves of the imaginary ($-Z''$) versus the real (Z') component of impedance were acquired at 120 °C in order to obtain the grain boundary resistance (R_{gb}) and capacitance (C_{gb}) assuming an RC equivalent circuit.

Results and discussion

Microstructural features

The X-ray powder diffraction patterns of the sintered samples showed no other phase besides cassiterite,

Table 1 Studied compositions (mol %)

Sample	SnO_2	Co_3O_4	Nb_2O_5	Al_2O_3
SCN	99.62	0.33	0.05	–
SCNA1	99.57	0.33	0.05	0.05
SCNA2	99.52	0.33	0.05	0.10
SCNA3	99.37	0.33	0.05	0.25

suggesting single phase systems within the detection limits of this technique. Figure 1 shows the microstructures observed with SEM and Table 2 presents the density, the average grain size and unit cell volume measured for each sample.

The possible charge compensation mechanisms in SnO_2 may involve conduction electrons, electron holes, oxygen vacancies and tin vacancies. However, it is known that electron holes in tin oxide are minority defects in comparison to oxygen vacancies [19]. Independently of the aluminium source, the possible substitution equations, where the Kröger-Vink standard notation is used, are:

$$Al_2O_3 \rightarrow 2Al_{Sn}{}' + V_O^{..} + 3O_O^x \tag{6}$$

$$Al_2O_3 \rightarrow 2Al_{Sn}{}' + 2V_O^{.} + 2O_O^x + {}^{1}\!/_{2}O_2 \tag{7}$$

$$V_O^{..} + e' \rightarrow V_O^{.}. \tag{8}$$
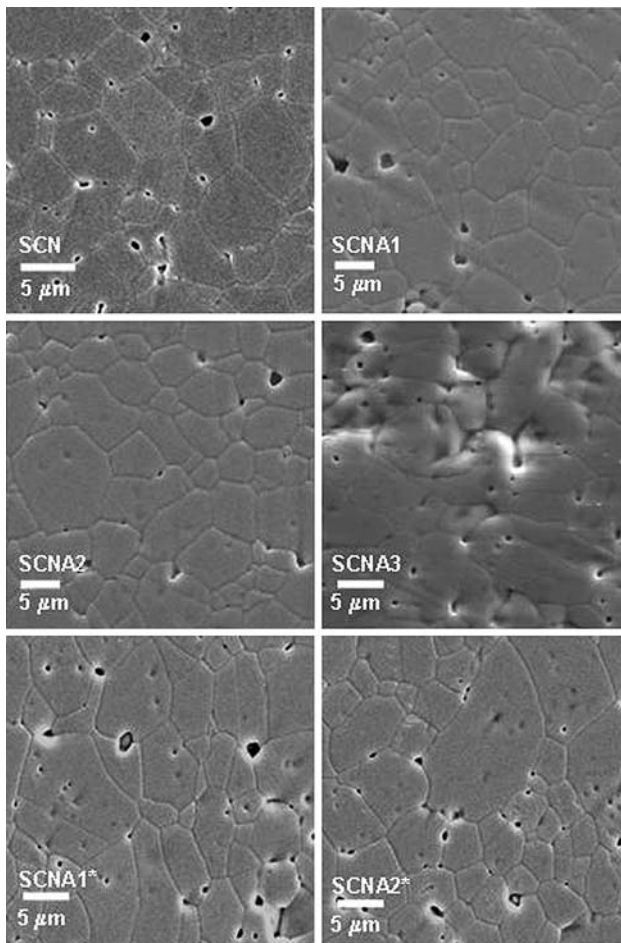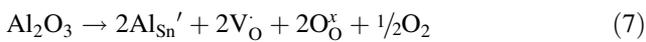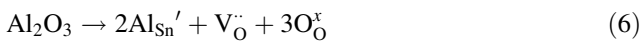
Fig. 1 SEM images of the sintered samples. AlO(OH) was the Al source for samples SCNA1* and SCNA2*

Thus, the solid solution formation would happen along with the creation of oxygen vacancies ($V_O^{..}$, $V_O^{.}$). However, due to the difference that exists between the ionic radii of Al^{3+} (0.51 Å) and Sn^{+4} (0.71 Å), the solid solution is not expected to occur in a great extent. Moreover, as shown in Table 2, the density of the SCN sample was not improved with the addition of alumina given that the concentration of oxygen vacancies was not sufficiently increased. The addition of Al_2O_3 in a concentration up to 0.05% mol led to a small increase in the average grain size and to a small reduction in the unit cell volume. Further additions of alumina caused a gradual decrease in d. On the other hand, the unit cell volume of samples SCNA2 and SCNA3 was increased with respect to that of the SCN sample. Summarising, the highest impact of Al_2O_3 on the microstructure was seen to occur with the addition of 0.25% mol of the oxide. With the addition of aluminium from AlO(OH) the mean grain size did not experienced significant changes, though a decrease in density was measured for sample SCNA1*. A higher density, around the 98% of the theoretical density, was obtained with a further addition of aluminium in sample SCNA2*. The formation of a substitutional solid solution of Al_2O_3 from the boehmite precursor in SnO_2 is evidenced in the decrease of the unit cell volume of both samples.

The occupation of interstitial sites is another alternative for aluminium. The following equations show that no further oxygen vacancies are introduced as the interstitial solid solution proceeds:

$$2Al_2O_3 \rightarrow 4Al_i^{...} + 3V_{Sn}{}'''' + 6O_O^x \tag{9}$$

$$V_{Sn}{}'''' + 2V_O^{..} \rightarrow 2V_O^{.} + V_{Sn}{}''. \tag{10}$$
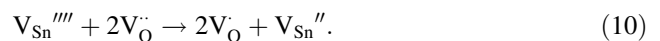
Nevertheless, this alternative seems rather difficult to be accomplished since it involves the creation of a tetravalent defect such as $V_{Sn}{}''''$ to compensate for each $Al_i^{...}$.

A deeper microstructural characterisation was carried out with EDS assisted TEM. Although particles of secondary phases other than SnO_2 were not detected with SEM (Fig. 1), the TEM images in Figs. 2 and 3 show precipitates containing Sn, Co, Al and O in their composition in samples with Al_2O_3 as well as in samples with Al_2O_3 from AlO(OH). The effect of precipitates on the electrical properties of SnO_2-based varistors has been studied but is not completely understood yet; however, their detrimental effects have been systematically reported [12–14]. In fact, these precipitates concentrate the species intentionally added to enhance the varistor properties. Figure 2 includes a high resolution TEM image of the grain boundary where the different orientation of the crystallographic planes on both sides of the boundary can be seen

Table 2 Apparent density (ρ), percentage of theoretical density (%ρ_t), average grain size (*d*) and unit cell volume (*V*) of the sintered samples

	ρ (g/cm^3)	% ρ_t	*d* (μm)	*V* (Å^3)
SCN	6.80	98.0	5.0	71.32
SCNA1	6.80	97.8	5.5	71.30
SCNA2	6.77	97.5	5.0	71.40
SCNA3	6.74	97.0	4.2	71.36
SCNA1*	6.75	97.0	4.7	71.23
SCNA2*	6.78	97.5	4.8	71.25

SnO$_2$ theoretical density: 6.95 g cm^{-3}

and, apparently, there is not an obvious insulating intergranular phase such as that observed in ZnO-based varistors. The electron diffraction patterns in Fig. 2 show that both the matrix and the precipitates belong to well crystallised single phase systems. Figure 2d corresponds to SnO$_2$ (cassiterite, JCPDS 41-1445) whereas Fig. 2e matches with the cubic system Co$_2$SnO$_4$ (JCPDS 29-0514), with a lattice parameter equal to 8.6376 Å, with aluminium incorporated into the structure.

Electrical properties

The major influence of the addition of aluminium to the SCN sample was seen to occur in the electrical behaviour. Table 3 and Fig. 4 show that the addition of Al$_2$O$_3$ did not alter the electrical behaviour of sample SCN. In fact, the electric breakdown field, the non-linearity coefficient and the number of electrically active barriers remained close to those of the SCN sample, what might be another evidence of the incapability of Al$_2$O$_3$ to form a solid solution with SnO$_2$. According to the number of electrically active barriers, the decrease in E_r with the addition of 0.05% mol of Al$_2$O$_3$ is only due to the larger grain size of this sample with respect to that of the sample without alumina. The variation of the grain boundary resistance (R_{gb}) of these samples can also be seen in Table 3 and in Fig. 5. At a glance, there arises a contradiction between some E_r and the R_{gb} values, since the lowest breakdown field and the highest grain boundary resistance correspond to the sample SCNA1. However, going back to Fig. 4 it can be seen that, at low electric fields, where the grain boundary characteristics dominate the conduction, the sample SCNA1 displayed the lowest current density. Even though the non-linearity coefficient was not enhanced, the R_{gb} increased with the addition of Al$_2$O$_3$ because of the segregation to the grain boundary regions of the alumina that does not form a solid solution. The rather constant values obtained for the grain boundary capacitance (C_{gb}) confirm that the electrical properties of the barrier voltage at grain–grain junctions were neither improved nor degraded. It is possible that, due to its remarkable chemical stability, the alumina added remains in the form of particles of minority phases with no influence whatsoever on the potential barrier.
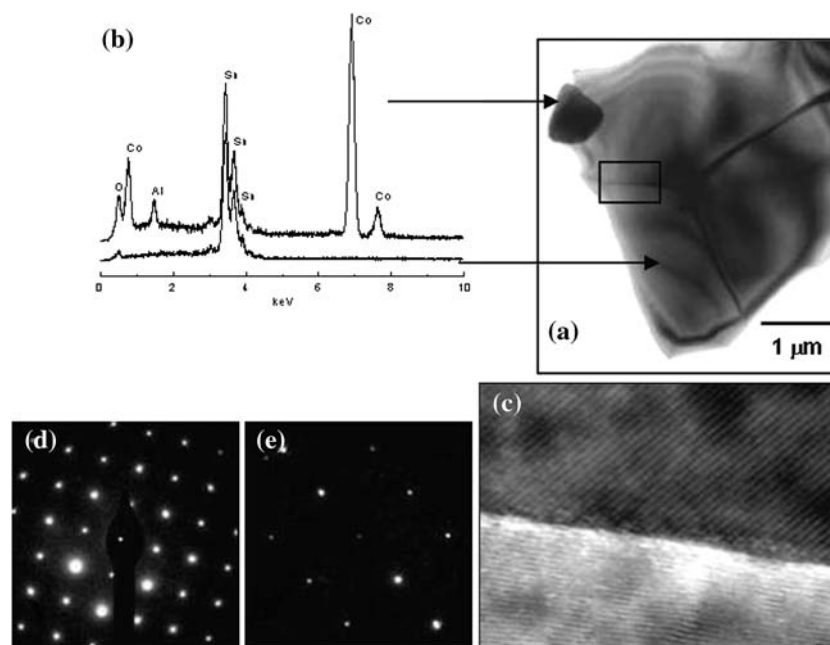
Fig. 2 (a) TEM image of sample SCNA2 including (b) the EDS analysis of the phases present, (c) the HRTEM image of the grain boundary (inset in (a)) that shows the absence of an insulating intergranular phase, and the SAED patterns of (d) the matrix matching for SnO$_2$ and of (e) the particle arrowed in (a) matching for Co$_2$SnO$_4$
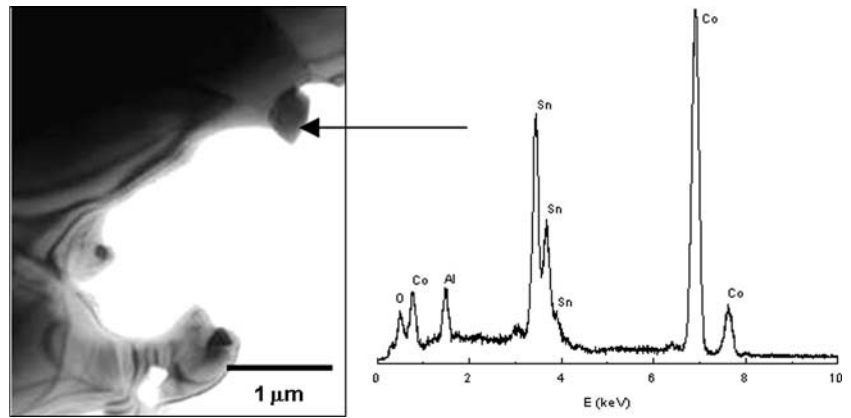
The samples SCNA1* and SCNA2* with the addition of aluminium from AlO(OH) showed a different electrical behaviour. An increase in the concentration of aluminium led to an enhanced non-linearity coefficient. The electric breakdown field, the percentage of electrically active barriers and the R_{gb} were as well increased. Moreover, the decrease in the C_{gb} stands for better voltage barrier properties. In a Schottky-type barrier, the capacitance is related to the donor concentration in the bulk, n, and to the barrier height, ϕ, as

$$C_{gb} \propto \left(\frac{n}{\phi}\right)^{1/2}. \qquad (11)$$

Then, a diminution in the capacitance may be due to an increase in the potential barrier height, to a decrease in the donor concentration or, eventually, to both phenomena occurring simultaneously [20]. Since, in agreement with the Eqs. 6–10, the concentration of donors is not supposed to diminish when the content of aluminium from AlO(OH) is increased the lower C_{gb} value can be ascribed to an increase in the barrier height. Even though a fraction of the aluminium added as AlO(OH) is involved in the formation

of a secondary phase, the variations observed in the microstructure and the improvement of the electrical properties may be attributed to the higher chemical reactivity of AlO(OH) against Al_2O_3 and to a more homogeneous distribution of Al^{3+} in the microstructure. The presence of aluminium, as well as other point defects, at grain–grain interfaces might be responsible for the higher R_{gb} and E_r of the samples with aluminium from boehmite. It can be concluded that Al^{3+} species are differently distributed in the SnO_2 network according to the source of aluminium.

Conclusions

The influence of two aluminium sources on the microstructure development and on the electrical properties of SnO_2-based varistors was clarified. Precipitates of

Table 3 Electric breakdown field (E_r), percentage of electrically active barriers (% EAB), non-linearity coefficient (α) and grain boundary resistance (R_{gb}) and capacitance (C_{gb}) of the sintered samples

	E_r (V/cm)	% EAB	α	R_{gb} (Ω)	C_{gb} (F)
SCN	2090	30	14	1.8×10^5	2×10^{-9}
SCNA1	1960	31	13	3.0×10^6	3×10^{-9}
SCNA2	2030	29	13	1.7×10^6	2×10^{-9}
SCNA3	2100	26	13	1.8×10^6	4×10^{-9}
SCNA1*	2430	33	12	4.8×10^6	2×10^{-9}
SCNA2*	3720	51	19	5.3×10^6	9×10^{-10}
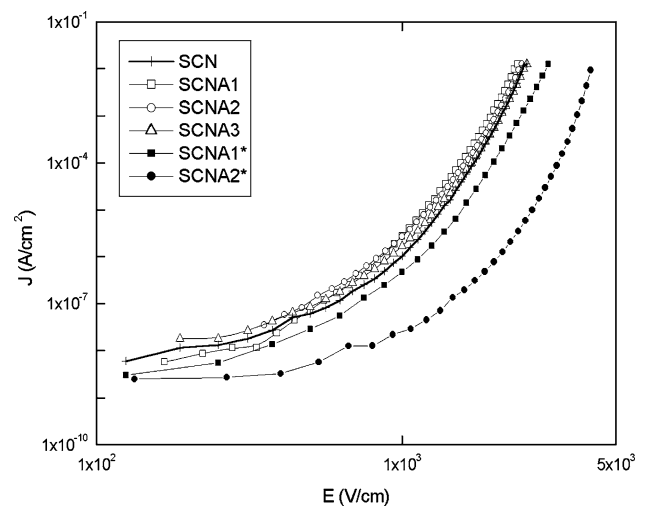
Fig. 4 J–E characteristics for the sintered samples registered at room temperature
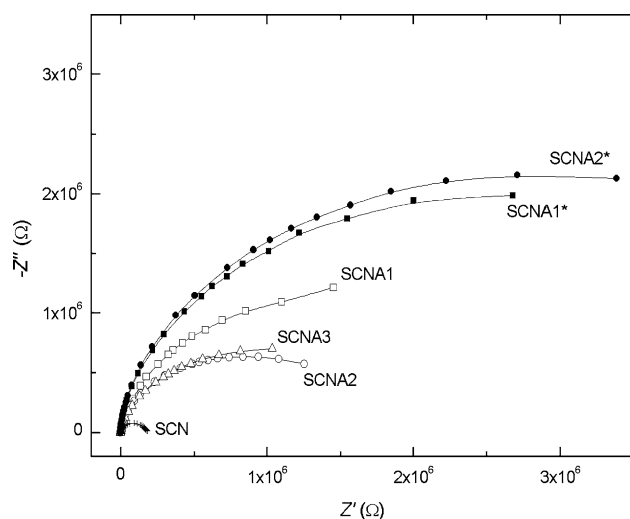
Fig. 5 Impedance spectroscopy curves for the sintered samples registered at 120 °C

Co_2SnO_4 with Al incorporated into the structure were found independently of the aluminium precursor. The different properties between the samples with aluminium from AlO(OH) and from Al_2O_3 were attributed to the higher reactivity of the former against the latter. The effects of Al_2O_3 on the electrical properties were seen to be negligible, whereas the addition of 0.10% mol of Al_2O_3 from boehmite led to a device with a non-linearity coefficient of 19 and with the highest electric breakdown field.

References

1. Gupta TK (1990) J Am Ceram Soc 73:1818
2. Matsuoka M (1981) In: Levinson LM (ed) Grain boundary phenomena in electronic ceramics. Advances in ceramics, vol 1. The American Ceramic Society Inc., Ohio, pp 290–308
3. Levinson LM, Philipp HM (1996) Am Ceram Soc Bull 85:639
4. Brankovic Z, Brankovic G, Poleti D, Varela JA (2001) Ceram Int 27:115
5. Kim CH, Kim JH (2004) J Eur Ceram Soc 24:2537
6. Pianaro SA, Bueno PR, Longo E, Varela JA (1995) J Mater Sci Lett 14:692
7. Castro MS, Aldao CM (1998) J Eur Ceram Soc 18:2233
8. Parra R, Varela JA, Aldao CM, Castro MS (2005) Ceram Int 31:737
9. Brito GES, Pulcinelli SH, Santilli CV, Barelli N (1993) J Mater Sci Lett 12:992
10. Varela JA, Perazolli LA, Longo E, Leite ER, Cerri JA (1998) Radiat Effect Defect Solid 146:131
11. Parra R, Aldao CM, Varela JA, Castro MS (2005) J Electroceram 14:149
12. Wang JF, Wang YJ, Su WB, Chen HC, Wang WX (2002) Mater Sci Eng B 96:8
13. Dhage SR, Ravi V, Date SK (2002) Mater Lett 57:727
14. Parra R, Castro MS, Varela JA (2004) J Eur Ceram Soc 25:401
15. Oliveira MM, Soares PC Jr, Bueno PR, Leite ER, Longo E, Varela JA (2003) J Eur Ceram Soc 23:1875
16. Simoes LPG, Bueno PR, Orlandi MO, Leite ER, Longo E (2003) J Electroceram 10:63
17. Mendelson MI (1969) J Am Ceram Soc 52:443
18. Leite ER, Nascimento AM, Bueno PR, Longo E, Varela JA (1999) J Mater Sci Mater El 10:321
19. Matei Ghimbeu C, van Landschoot RC, Schoonman J, Lumbreras M (in press) J Eur Ceram Soc 27:207
20. Castro MS, Aldao CM (1997) J Eur Ceram Soc 17:1533